International Journal of Multiphase Flow 167 (2023) 104497

Contents lists available at ScienceDirect

International Journal of Multiphase Flow

journal homepage: www.elsevier.com/locate/ijmulflow

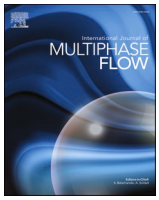

Effect of injector geometry in breakup of liquid jet in crossflow – insights from POD

Anubhav Sinha

Indian Institute of Technology (Banaras Hindu University), Varanasi 221005, India

A B S T R A C T

The present study investigates the role of injector geometry, particularly injector tube length-to-diameter ratio (L/D), in liquid jet stability and breakup in the presence of crossflow. Water is injected into a crossflow of air. Aerodynamic Weber number (We_g) and liquid Reynolds number (Re_l) are systematically varied to observe various breakup modes. High-resolution images are captured for the near-nozzle region. Transition to turbulence is found to be affected by the nozzle geometry. Column breakup and surface stripping are observed for different operating conditions. A regime map is proposed based on the present observations. Time-resolved jet trajectory images are processed using Proper Orthogonal Decomposition (POD) algorithm. POD mode shapes and corresponding Power Spectral Density (PSD) plots are analyzed to study the breakup process and probe the role of injector geometry effects. A detailed comparison is made for various cases. It is observed that with an increase in (L/D), the jet surface becomes more turbulent and unstable, which results in an early breakup and lower jet penetration.

1. Introduction

Liquid Jet in crossflow (LJIC) is an important configuration for fuel injection in aerospace applications, particularly in gas turbine engines, afterburners, and ramjets. A liquid jet is injected into a crossflow of high-velocity airflow. The jet disintegrates into ligaments and drops. The breakup is understood to be caused by aerodynamic forces. Aerodynamic forces start acting on the jet's surface as the jet enters the crossflow. However, liquid turbulence and jet instability also aid the breakup process. Ligaments and drops formed from primary breakup further undergo secondary breakup to produce smaller droplets which eventually evaporate, mix, and combust. Jet breakup and droplet formation impact fuel mixing, combustion efficiency, and pollutant formation. It could also play a significant role in thermo-acoustic instabilities and their control. Hence, it becomes crucial to understand the breakup process and the factors which govern it. Aerodynamic Weber number (We_g) is an essential parameter for LJIC configuration, which is defined as:

$$We_g = \frac{\rho_g U_g^2 D}{\sigma} \tag{1}$$

where ρ_g is the gas density, U_g is the gas velocity, D is the jet diameter, and σ is the surface tension. For lower We_g, the column bends, gets flattened and breaks undergoing column or bag breakup. For larger We_g, surface stripping is observed, and the jet undergoes a more rapid breakup. Instantaneous images of jets undergoing different breakup modes are presented in Fig. A1 in Appendix. Wu et al. (1997,1998) carried out a detailed investigation of LJIC for a wide range of operating conditions and classified different regimes of jet breakup using jet instantaneous images. Their regime map is based on We_g and jet to crossflow momentum flux ratio (q), where q is defined as:

$$q = \frac{\rho_l U_l^2}{\rho_g U_g^2} \tag{2}$$

where ρ_g is the gas density, U_g is the gas velocity, ρ_l is the liquid density, and U_l is the liquid velocity. The injector used by (Wu et al., 1997, Wu et al., 1998) had a fixed Length-to-Diameter (L/D) ratio of 4. Mazallon et al. (1998) investigated LJIC using different jet liquids and operating conditions. They conclude We_g to be the controlling parameter in the jet breakup and relatively minor effect from q. Another study was conducted by (Sallam et al., 2004). They have also studied different breakup regimes for nonturbulent jets and plotted their observation on a regime map. They concur that We_g is the determining factor for laminar jets, and q or Re_l (liquid Reynolds number) has no significant impact on the jet breakup. Ng et al. (2008) conducted a detailed experimental study characterizing the column and bag breakup regimes. They used a super-cavitating nozzle to generate a nonturbulent jet. They have analyzed bag formation and its rupture. The jet instability is attributed to Rayleigh-Taylor instability. They have derived relations for surface waves and found a good match with their experimental observation. Lee et al. (2007) have undertaken an experimental study of turbulent jet breakup in the presence of crossflow. They focused on the role of liquid turbulence in the jet breakup, in contrast to previous studies which

E-mail address: er.anubhav@gmail.com.

https://doi.org/10.1016/j.ijmultiphaseflow.2023.104497
Received 4 June 2022; Received in revised form 9 April 2023; Accepted 20 April 2023
Available online 22 April 2023

Nomenclature

L	injector tube length
D	injector/ jet diameter
Re	Reynolds number
We	Aerodynamic Weber number
q	Momentum flux ratio of jet and crossflow
Fa	Faeth number
U	velocity
ρ	density
σ	surface tension
u'_{rms}	RMS turbulence fluctuations in velocity
Subscripts	
g	gas phase
l	liquid phase

focused on aerodynamic effects. A general agreement is that increasing air velocity (resulting in higher We_g) enhances the breakup. However, (Lee et al., 2007) suggested that the breakup is primarily caused by jet turbulence, and it gets suppressed by increasing air velocity on the windward side. Sallam et al. (2006) experimented on both laminar and turbulent jets and compared breakup regimes. They have investigated the role of jet turbulence in jet disintegration. They have introduced a new non-dimensional number, Faeth number (Fa), to characterize the breakup of turbulent jets. Faeth number is defined as:

$$Fa = We_l \cdot q^{1/3} \tag{3}$$

where q is the momentum flux ratio, and We_l is the liquid Weber number, defined as:

$$We_l = \frac{\rho_l U_l^2 D}{\sigma} \tag{4}$$

where ρ_l is the liquid density, U_l is the liquid velocity, D is the jet diameter, and σ is the surface tension. They argue that turbulent eddies in the jet are primarily responsible for the breakup in the turbulent breakup regime. If the crossflow air velocity increases, the pressure force on the jet increases and suppresses breakup.

The injector used by (Mazallon et al., 1998) and (Sallam et al., 2004, Sallam et al., 2006) focused on the non-turbulent jet and they used an injector with lower L/D ($L/D < 3$). In contrast, (Lee et al., 2007) and (Sallam et al., 2006) have used an injector with (L/D)>100 and generated a turbulent jet. It is important to note that this understanding was there that (L/D) impacts jet stability and transition to turbulence (McCarthy and Molloy, 1974, Wu et al., 1995), but no comprehensive study was undertaken to explore this aspect in LJIC. Madabhushi et al. (2006) have reviewed previous studies on jet breakup regimes. They have highlighted that the momentum flux ratio (q) can be replaced by liquid Reynolds number (Re_l) in regime maps and emphasized that Re_l offers more physical insight, as the jet transition from laminar to turbulent can be captured by the value of Re_l. It is also observed that the effect of injector geometry is overlooked in the available literature. Brown and McDonell (2006) have captured near-nozzle images of jet breakup in crossflow. They observed jet trajectories captured in their experiments in good agreement with correlations available in the literature (Wu et al., 1998, Stenzler et al., 2006). Interestingly, they admitted that they get a good match because they have injector geometry similar to what was used to derive those correlations. They also suggested that the role of injector geometry needs to be studied in detail.

Due to the practical significance of LJIC, this configuration has been a subject of active research for decades (Broumand and Birouk, 2016, Mashayek and Ashgriz, 2011). However, there is no general agreement on something as fundamental as a regime map for the breakup or the parameters that govern the breakup (Broumand and Birouk, 2016). The boundaries between different regimes vary in each study, depending on their test conditions and injector geometry used (Madabhushi et al., 2006). Even for jet trajectory and penetration, numerous correlations are available in the literature focusing on different parameters (Mashayek and Ashgriz, 2011, No, 2015). This could partly be attributed to neglecting the effect of injector geometry in previous literature. Injector geometry is considered so insignificant that several papers haven't even provided all the geometry details regarding their injector (Madabhushi et al., 2006). A recent study (Sinha, 2019) investigated the effect of L/D on LJIC. However, that study entirely focused on wave growth on the jet surface, and the jet breakup was not investigated. Some experimental investigations (Gong et al., 2019, Portillo et al., 2011) focus on the role of injector geometry in the generation of surface waves on liquid jets. They have characterized wavelength and studied the transition to turbulence for a liquid jet discharged into a quiescent ambient. Portillo et al. (2011) have attributed the transition to turbulence to the instability near the nozzle exit. However, this aspect remains unexplored, particularly for LJIC configuration.

LJIC configuration has also been investigated using computational tools, where several critical physical processes are captured in numerical simulations. Behzad et al. (2016) have carried out a numerical study of LJIC for high-pressure conditions. They have captured surface waves and droplet stripping from the jet at high We_g cases. They have kept Re_l low to obtain a laminar jet. Herrmann (2010) has carried out numerical simulations for the conditions of (Brown and McDonell, 2006) and was able to capture jet primary breakup characteristics for a turbulent jet. In this study, internal injector flow is also simulated, and injector-induced instability is captured, generally neglected in other numerical studies (Li and Soteriou, 2016, Tretola et al., 2021).

Another noteworthy point is that breakup in JICF configuration is a highly unsteady process. It has been pointed out by various researchers (Madabhushi et al., 2006, Brown and McDonell, 2006) that a single instantaneous image per case is not sufficient to investigate various breakup modes, their associated structures, and frequencies. Time-resolved videos or a large set of images are generally needed to understand the dynamics of this configuration. Time resolution for image capture is determined by the highest frequency observed in the flow field, which typically leads to thousands of frames per second. Hence, to understand the breakup process for one case, a large set of instantaneous images need to be analyzed. Another alternative is to process these images using Proper Orthogonal Decomposition (POD) analysis. POD is a data reduction technique used to obtain low-dimensional approximations of high-dimensional data. Berkooz et al. (1993) have explained the basics of POD analysis with its applications. Liang et al. (2002), Taira et al. (2017), Taira et al. (2020), and Sirovich (1987) have also detailed the basic mathematical principles and applications of POD. The present work uses snapshot POD. Taira et al. (2017,2020) have compiled a valuable reference for POD and other modal reduction techniques, along with applications from fluid mechanics. POD is handy for identifying coherent structures in fluid flow and their associated frequencies. POD was recently used to investigate airblast spray dispersion in crossflow (Sinha and Ravikrishna, 2019), and a regime map was proposed based on POD analysis. Arienti and Soteriou (2009) explore the applicability of POD to study JICF configuration. However, the complex nature of jet breakup and the ability of POD to identify hidden structures warrant more research to be devoted to this topic.

To summarize, there is a need to identify the role of injector geometry in jet breakup in crossflow. It requires both spatial and time-resolved imaging to gain a complete understanding of the complex physics of jet breakup. Also, POD is a tool that can help identify hidden structures in fluid flow problems and has not been fully utilized in JICF configuration. This paper attempts to address this issue.

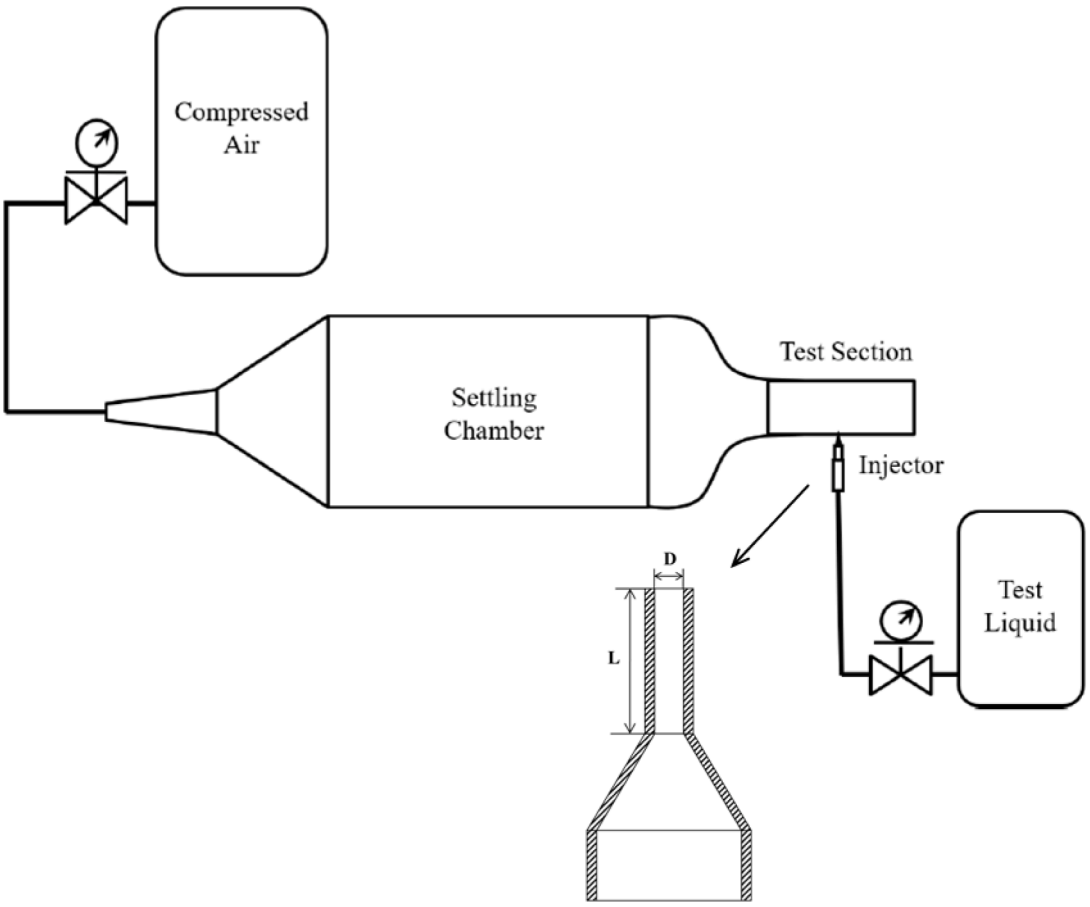

Fig. 1. Schematic of Experimental facility. Injector geometry details are shown in an enlarged image.

2. Experimental Details

2.1. Experimental setup

The experimental setup consists of an air supply system for the crossflow air and a liquid supply system for the injector. A schematic of the facility is shown in Fig. 1. The air supply is a blowdown type of wind tunnel. Air is stored in tanks at high pressure. After being released from the tanks, air passes through control valves, diverging section, settling chamber, and finally through a converging section to the test section. The converging section is designed following the guidelines of (Mehta and Bradshaw, 1979) and (Brassard and Ferchichi, 2005). The velocity profile and turbulence levels are characterized using a hot wire anemometer at the entry of the test section. The velocity profile is quite uniform, with the velocity values varying within 2.5% of the mean. The turbulence intensity (u'_{rms}/U) is measured to be around 3%. Details about the velocity profile and turbulence measurement are provided elsewhere (Sinha et al., 2015).

The test section is a rectangular duct of 50 mm X 54 mm cross-section and 250 mm in length. It is made optically accessible by quartz side-walls. The injector is flush-fitted to the center of the bottom wall. The injector diameter (D) is fixed to 0.5 mm, and the tube length (L) is varied to obtain (L/D) ratios of 10 and 100. A Coriolis-based mass flow controller governs the liquid supply to the injector (Make: Bronkhorst, Model: mini-Cori-Flow, Accuracy: ±0.2% of flow rate).

2.2. Imaging systems

The present study uses two imaging systems: near-nozzle spatially-resolved imaging, and time-resolved trajectory imaging. Near-nozzle

Table 1
Test conditions of the cases considered in this study.

Case	L/D Ratio	Jet Reynolds number (Re_l)	Momentum Ratio (q)	Aerodynamic Weber Number (We_g)
J1-10	10	2545	11.2	16.2
J1-100	100	2545	11.2	16.2
J2-10	10	5090	44.7	16.2
J2-100	100	5090	44.7	16.2
J3-10	10	5090	22.3	32.3
J3-100	100	5090	22.3	32.3
J4-10	10	5090	12.9	55.9
J4-100	100	5090	12.9	55.9
J5-10	10	7635	29.1	55.9
J5-100	100	7635	29.1	55.9
J6-10	10	10180	36.4	79.4
J6-100	100	10180	36.4	79.4

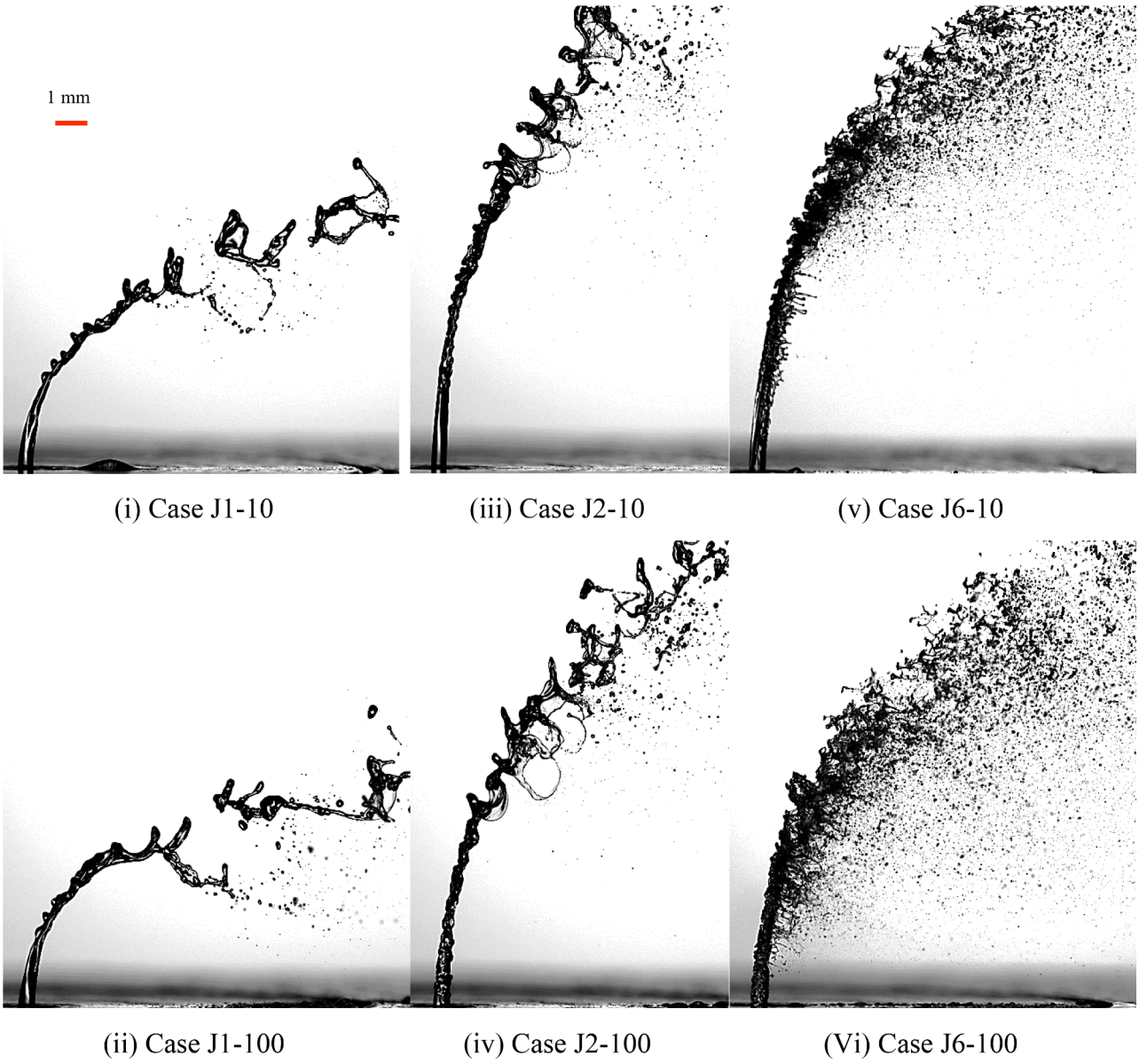

Fig. 2. Instantaneous images for some sample cases considered in this study. The first row shows L/D 10 cases, and the second row shows the corresponding L/D 100 cases.

images are captured using a 4MP CCD camera (LaVison, ImagerProX4M). A pulsed laser (model: Nano-L-200-15-PIV) is used in this system. The laser pulse is around ten nanoseconds. However, the laser falls on a diffuser plate with Rhodamine dye, fluorescing for around 20 nanoseconds. This diffuser plate is used for background illumination and gives an effective exposure time of 20 nanoseconds for the CCD camera. Due to superior background illumination from the laser system and such a small exposure time, the images obtained appear frozen in time and show detailed jet breakup morphology.

This system captures images at 120 pixels per mm for the settings used in this study. Although this imaging system provides a very high spatial resolution, the temporal resolution is limited by the laser repetition rate, which is 15 Hz. A high-speed CMOS camera (model: Photron Fastcam SA5) is used in conjugation with a DC-powered 500W halogen lamp for temporally resolved images of jet trajectory and breakup. Images are captured at 10,000 frames per second, with an exposure time of 1 microsecond and 30 pixel/ mm spatial resolution. The Nyquist frequency is, hence, 5000 Hz.

2.3. Experimental conditions

The test conditions for various cases investigated in this study are summarized in Table 1. For each pair of cases, the operating conditions are maintained the same, while (L/D) changes from 10 to 100. Liquid Reynolds number (Re_l) is kept under laminar conditions for the first pair (J1 and J2), near-critical value for the second pair (J3 and J4), and in the turbulent regime for the third pair (J5 and J6). The critical value of Re_l is defined as 5000 by (Madabhushi et al., 2006) for laminar to turbulence transition. The first two pairs are at a low We_g of 16, and the last pair is at a relatively higher We_g of 79. The momentum ratio varies from 11 to 45. Typical instantaneous images for some cases are shown in Fig. 2. The first row (Fig. 2(i), (iii), and (iv)) shows the L/D 10 cases, while the second row (Fig. 2(ii), (iv), and (vi)) shows the L/D 100 cases.

2.4. POD Analysis

Proper Orthogonal Decomposition (POD) is a data processing technique that is useful in identifying dominant structures and their asso-

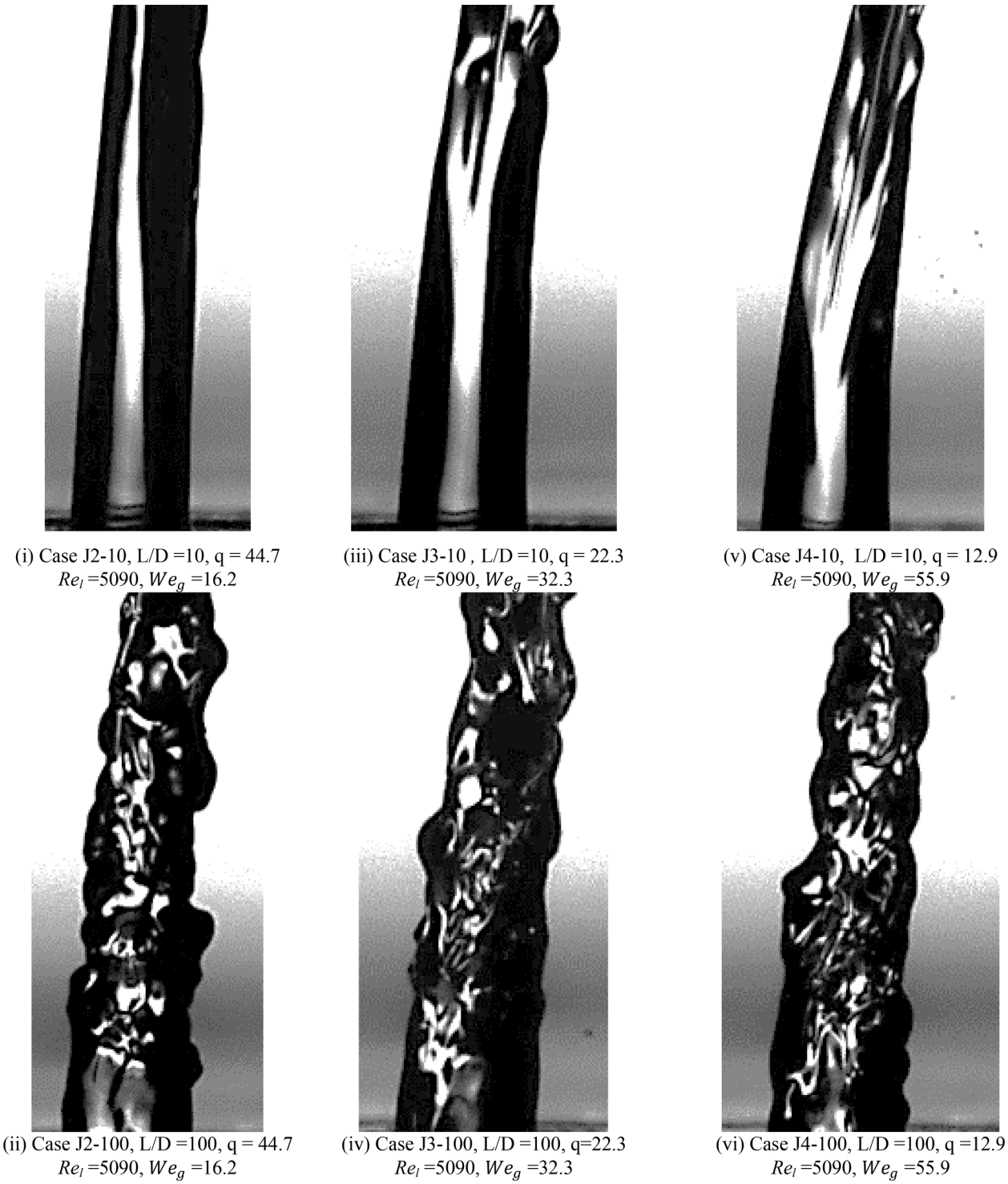

Fig. 3. Near nozzle image for various cases (for a constant Re_l). The first row shows cases with L/D=10, and the second row shows cases with L/D=100. The jet diameter is 0.5 mm.

ciated frequencies in a flow field. It is known by several names, viz. Principal Component Analysis (PCA), Karhunen-Love transform, etc. It has been demonstrated to be useful in fluid mechanics and turbulence in identifying coherent structures and revealing hidden patterns in a flow field. Consider a random field $z(x,t)$ which can be expressed in a variable separable form:

$$z(x,t) = \sum_{j=1}^{\infty} a_j(t)\ \varphi_j(x) \tag{5}$$

Now, this representation is not unique. Any random function φ_j can be chosen, and that will determine the a_j's. The question is what the best way is to choose φ_j ? The POD procedure involves selecting an orthonormal basis function for φ_j, such that the coefficient a_j is only dependent on φ_j. Further, the coefficients φ_j are arranged in such an order that the first j terms are the best possible j-term approximation of Eq. (5). The coefficient φ_j is considered to be the coefficient for space and gives the POD modes. Coefficient a_j is then the time coefficient. A Fourier transform of a_j provides the PSD plots containing frequency information. The

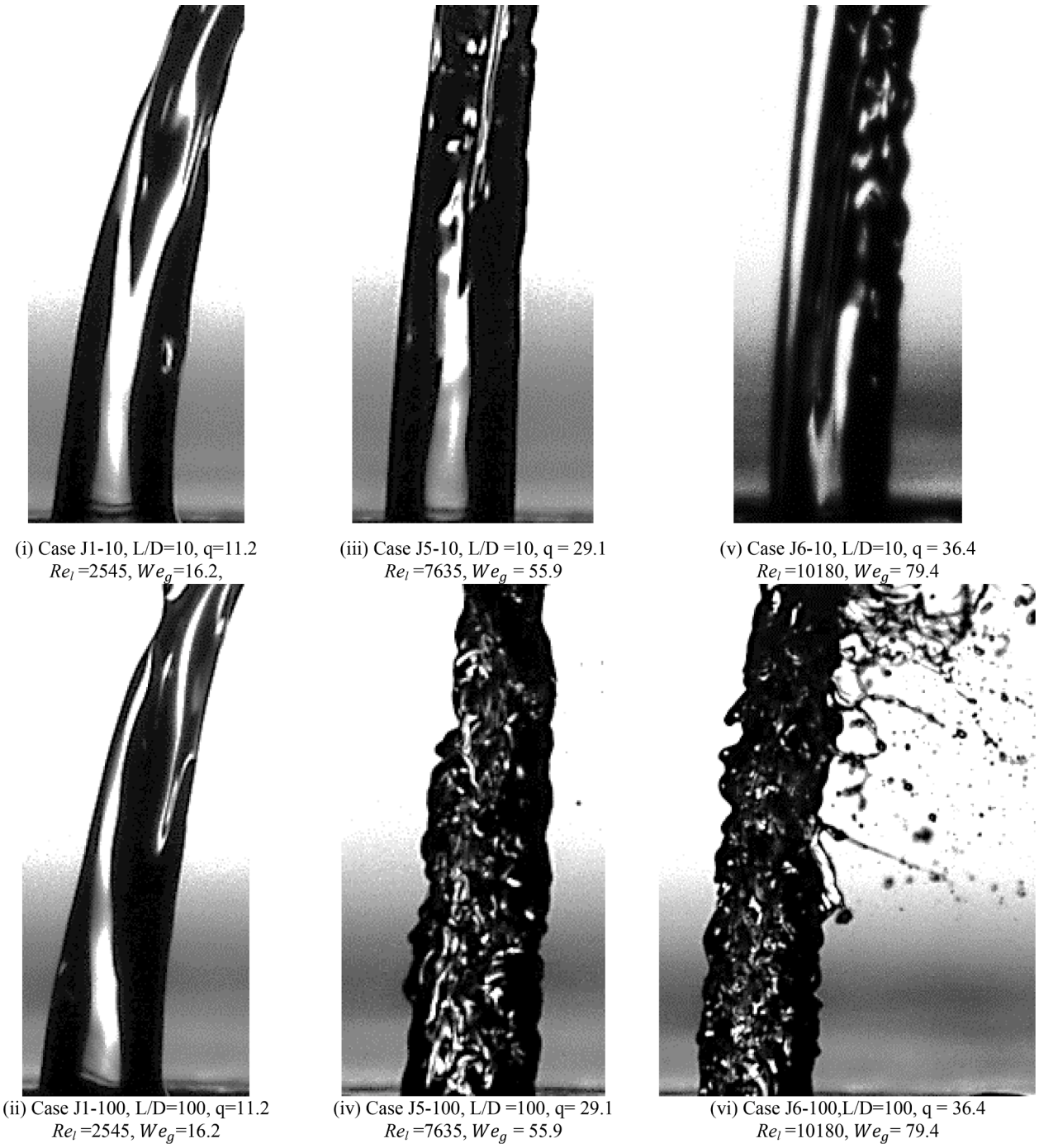

Fig. 4. Near nozzle image for various cases. The first row shows cases with L/D=10, and the second row shows cases with L/D=100.

POD procedure is briefly explained in the following paragraph.

Time-resolved images are captured for POD analysis. Pixel values from each image are rearranged to form a column of matrix A. Matrix A contains the complete spatiotemporal information captured during an experiment. It can be decomposed into three matrices, following Singular Value Decomposition (SVD):

$$A = U\ \Sigma\ V^T \tag{6}$$

where U contains orthogonal spatial modes. Σ is a diagonal matrix that contains the corresponding modal energies. V^T is a transpose matrix that contains temporal information. Parallels can be drawn between Eqs. (5) and (6). Matrix A from Eq. (6) can be assumed to represent z from Eq.(5). The term $U\ \Sigma$ corresponds to φ_j and V^T can represent the temporal coefficient a_j. In the present study, snapshot POD is used (Sirovich, 1987). Instantaneous jet images are the input for the POD algorithm. The POD modes are arranged in descending order of their modal energies. The energy here refers to the variance from the mean flow field. The higher the energy, the closer the mode is to the mean flow field.

POD analysis was performed for 1000 images, which is generally considered to be a sufficiently large dataset. In terms of physical time, it represents 0.1 seconds. Moreover, an additional study was also conducted to assess the dependence of POD results on the number of images. It is observed that the POD results do not differ in the range of 100 to 3000 images for the given cases. For further details on the POD algorithm and its applications, the reader is referred to (Berkooz et al., 1993,

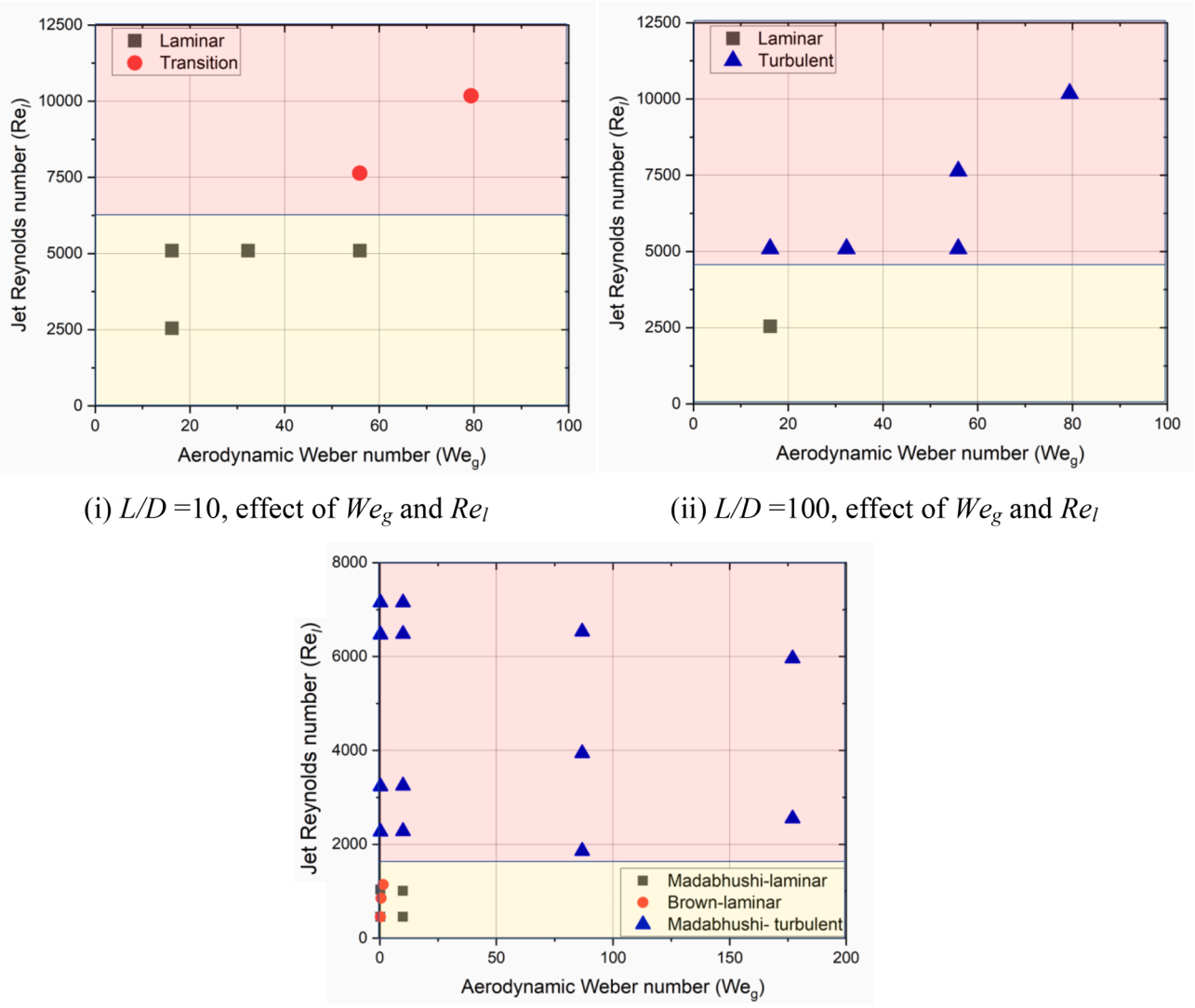

Fig. 5. Near nozzle behavior of liquid jets in crossflow configuration. Laminar, turbulent, and transition cases are shown for (i) L/D 10 injector, (ii) L/D 100 injector, and (iii) Cases from references (Madabhushi et al., 2006) and (Brown and McDonell, 2006).

Liang et al., 2002, Taira et al., 2017, Taira et al., 2020, Sirovich, 1987). One major disadvantage of POD is that each POD mode is made up of a mixture of different frequencies, as shown in PSD plots in the following sections. To obtain pure frequency modes, Dynamic Mode Decomposition (DMD) analysis can be used. However, in this study, POD modes appear to be more useful in identifying hidden dominant structures. DMD modes mostly capture small-scale features, and some sample results are shown in Appendix A (Fig. A2). More details about the DMD algorithm and applications can be found in (Schmid, 2010).

3. Results and discussion

3.1. Results

Fig. 3 shows the near-nozzle images for cases with Re_l near-critical value (Re_l =5090). The first row shows cases with L/D=10 and the second row depicts corresponding L/D=100 cases. Operating conditions are maintained constant for each column in the table, only the injector *(L/D)* is varied. As evident, jets in the first row appear laminar (having a glassy appearance). J2-10 (Fig. 3 (i)) appears the most stable, with a glassy appearance till the top of the image. A wave-like disturbance begins to appear near the top right corner. The origin of this disturbance shifts upstream from J2-10 (Fig. 3 (i)) to J4-10 (Fig. 3(v)). On the other hand, the corresponding cases in the second row (Fig. 3 (ii, iv), and (vi)) exhibit highly corrugated (or turbulent) jets. Although each case has a different crossflow air velocity, all the jets appear to be similar. It can be inferred that the injector geometry determines the jet structure and morphology in the near-nozzle region, and crossflow air has little or no effect. To further probe the effect of injector geometry, near-nozzle images of the jet without crossflow are shown in Appendix A (Fig. A2). Re_l is fixed to 5090 for all these cases and injector L/D is varied. As evident, the jet appears laminar at the nozzle exit for L/D=10 (Fig. A2(a)), but some disturbance is also observed on the jet surface. These disturbances shift near the nozzle exit with an increase in L/D ratio (Fig. A2(b)), and beyond L/D=50, the jet is turbulent right at the nozzle exit (Fig. A2(c,d)).

Another set of cases is compared in Fig. 4. Again, the first row shows cases with L/D= 10 and the second row is for L/D of 100. Re_l increases as one move from left to right. The effect of increasing Re_l is observed on the jet surface. J1-10 (Fig. 4 (i)) remains laminar till the top maintaining a clear glassy appearance. The wave-like disturbance observed in Fig. 3 is also observed in these images, although more enhanced, especially in

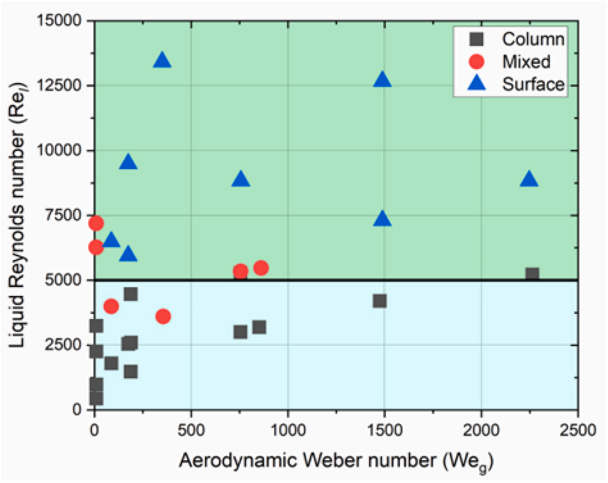

(i) Regime map from Madabhushi et al., 2006

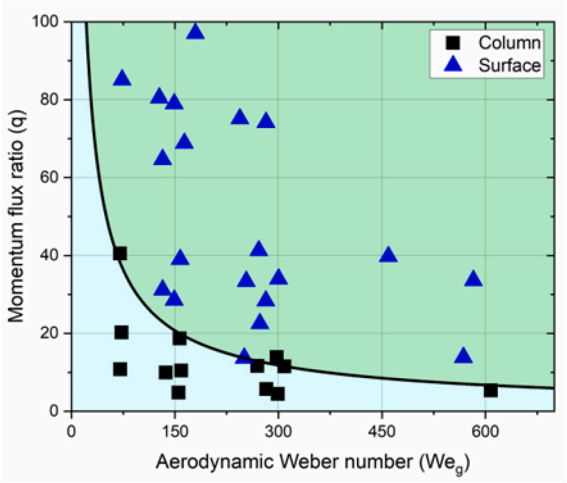

(ii) Regime map from Wu et al., 1997

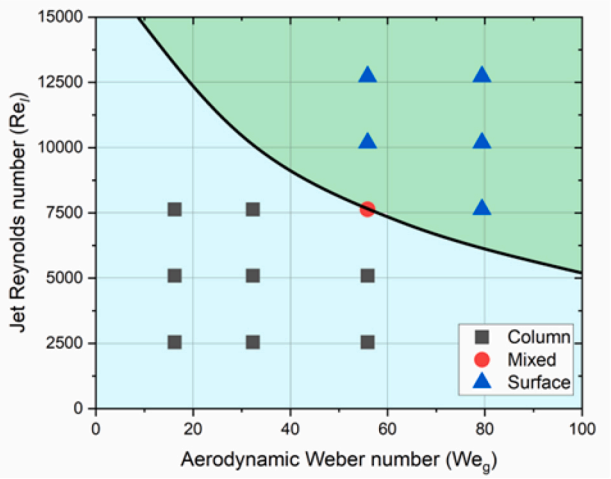

(iii) Regime map from present experiments

Fig. 6. (i) Regime maps (a) from (Madabhushi et al., 2006), (b) from (Wu et al., 1997), (c) based on the present experiments. Cases are divided into Column and Surface breakup regimes.

case J6-10 (Fig. 4 (v)). Interestingly, the wave appears only at the leeward side of the jet while the windward side appears to be stable for J6-10 in the near-nozzle region. The effect of increasing Re_l is strongly felt in the second row. While J1-100 (Fig. 4 (ii)) is laminar, J5-100 (Fig. 4(iv)) and J6-100 (Fig. 4 (vi)) are highly turbulent. J6-100 even exhibits a violent breakup with crossflow air stripping droplets and ligaments from its sides. In contrast, J6-10 (Fig. 4 (v)). which has the same operating conditions as J6-100 does not show any sign of breakup or droplet formation. J6-10 shows a glassy jet and wave formation downstream, rather than the turbulent corrugations seen on J6-100. This observation further validates the dominant role of injector geometry over crossflow in determining jet breakup in the near nozzle region. The second row shows a highly corrugated jet surface signifying turbulent characteristics. The surface corrugation observed for J5-100 (Fig. 4 (iv)) and J6-100 (Fig. 4(vi)) exhibit smaller length scales than those found in J3-100 (Fig. 3 (iii)) and J4-100 (Fig. 3 (vi)). This can be attributed to the higher Re_l for J5-100 and J6-100, and hence higher turbulent intensities.

To gain a further understanding of jet behavior, and its dependence on operating parameters, jet cases are classified as laminar and turbulent. Some L/D 10 cases which show intermittent behavior are marked as transitional. This classification is presented in Fig. 5 using Re_l vs We_g plots. Fig. 5(i) highlights the effect of We_g and Re_l for L/D=10 cases. Fig. 5 (ii) shows the effect of We_g and Re_l for L/D=100. Fig. 5 (iii) shows cases from the literature (Madabhushi et al., 2006, Brown and McDonell, 2006). The Re_l - We_g region is divided into laminar, turbulent, and transition regimes based on experimental observations. L/D 10 injector shows no turbulent case and L/D 100 injector shows no transitional case. L/D 10 jets are mostly limited to the laminar regime. For L/D 100 cases, except for the lowest Re_l case, all cases show turbulent characteristics. The above observation further validates the dominant role of injector geometry in the near nozzle region. Previous literature on LJIC is focused on jet trajectory and penetration. Magnified near-nozzle views of the jet surface are rarely reported. Near-nozzle jet images with sufficient resolution are reported by Madabhushi et al. (2006) and Brown and McDonell (2006). These images are examined and categorized into different regimes and shown in Fig. 5 (iii). They show similar trends as seen in the present study. For the present experiments, laminar to turbulent transition takes place around Re_l = 6000 for L/D 10 cases and around Re_l =5000 for L/D 100 cases. However, this transition observed in (Madabhushi et al., 2006) and (Brown and McDonell, 2006) is around Re_l =2000. This observation again stresses the role of injector geometry and internal flow conditions. This also highlights the novelty of the present work in probing jet surfaces using high-resolution near-nozzle images.

The impact of operating conditions on jet breakup modes is an active

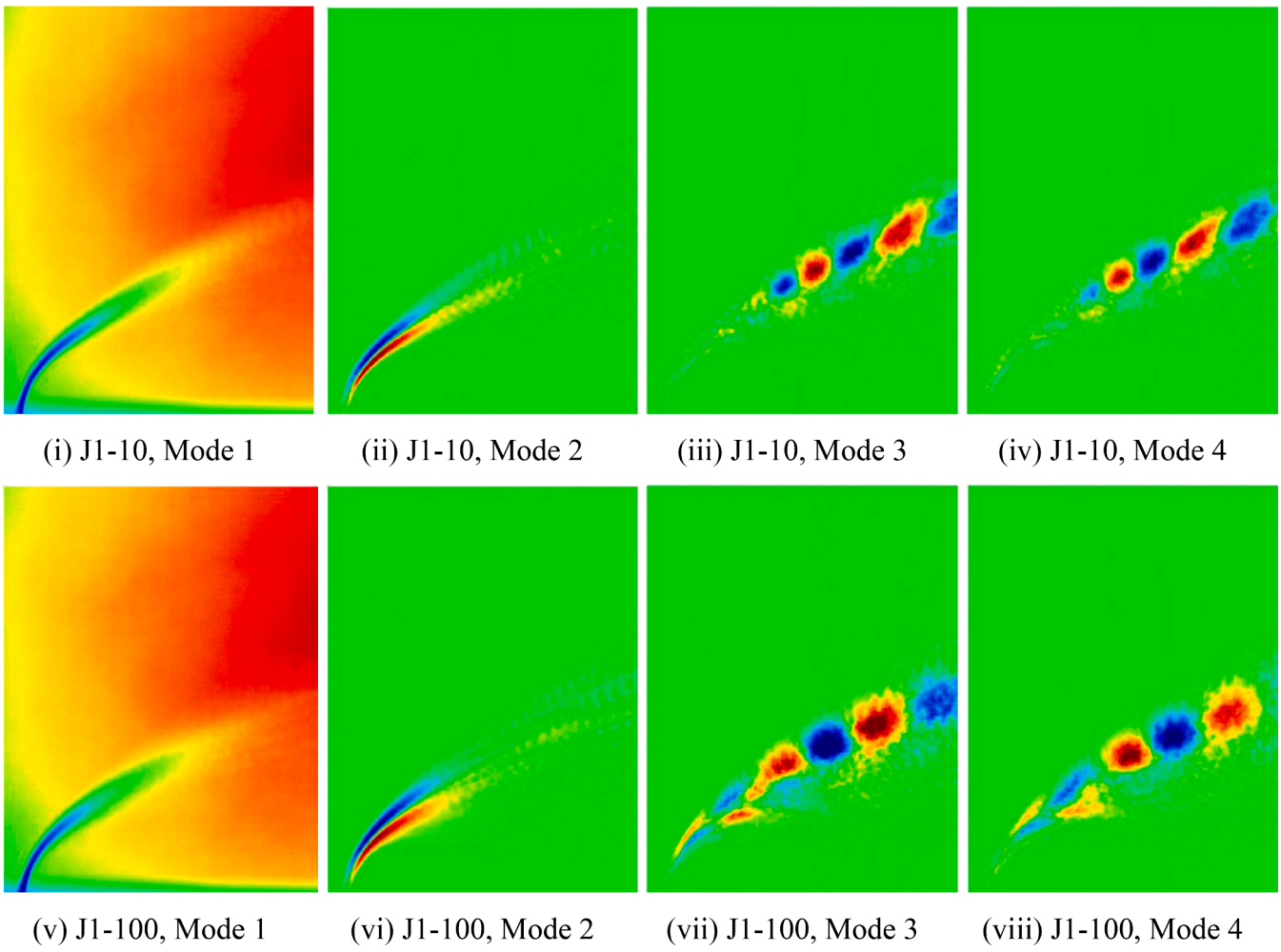

Fig. 7. POD Mode shapes for J1-10 and J1-100 cases.

area of research, and various researchers (Wu et al., 1997, Ng et al., 2008, Madabhushi et al., 2006) have attempted to classify the observed breakup behavior in different regimes. Typical examples of breakup mode regimes are shown in Fig. A1 of the Appendix. Column breakup mode is shown in Fig. A1(a), and bag breakup mode is depicted in Fig. A1(b). These two modes fall under column breakup regime. Multimode and surface breakup regime is shown in Fig. A1(c) and A1(d) respectively.

Aerodynamic Weber number (We_g) is traditionally believed to be the governing parameter for jet breakup in LJIC configuration (Wu et al., 1997, Wu et al., 1998, Mazallon et al., 1998). Some recent studies also emphasize the role of Re_l in jet breakup (Madabhushi et al., 2006). Madabhushi et al. (2006) proposed a jet breakup regime map in We_g - Re_l parametric space. The proposed regime map is shown in Fig. 6 (i) based on the results from (Brown and McDonell, 2006) and (Becker and Hassa, 2002). They have designated $Re_l = 5000$ as the boundary between column and surface breakup regimes. It is interesting to note that they have attributed the regime change solely to Re_l and rejected the effect of We_g. This is in stark contrast to previous literature (Wu et al., 1997, Ng et al., 2008), where We_g is a governing parameter. The regime map from (Wu et al., 1997) presented in Fig. 6 (ii) is in We_g -q parametric space.

To define the regime boundaries, the triggering of jet instability appears to be a crucial event, which is influenced by Re_l, as explained by (Madabhushi et al., 2006) and demonstrated in Fig. 4. Whereas (Wu et al., 1997) preferred momentum ratio (q) which is the ratio of jet to crossflow momentum. Jet momentum is accounted for in Re_l, and crossflow momentum can be linked to We_g. Hence, it appears, Re_l might be more fundamental than q for defining regime boundaries, as postulated by (Madabhushi et al., 2006).

To further investigate the role of We_g and Re_l, several LJIC cases are considered. Spatially resolved images are captured and associated breakup regimes are identified by visual inspection. LJIC cases are classified into column and surface breakup regimes and are presented in Fig. 6 (iii). Now, as per the classification of (Madabhushi et al., 2006), the breakup regime is only dependent on Re_l. Whereas in the present experiments, for Re_l=7635, all regimes (column, surface, and mixed) are obtained by varying the We_g (cf. Fig. 6(iii)). This observation makes it imperative to consider the effect of We_g in defining regime boundaries. In general, column breakup is observed for lower values of We_g and Re_l. While at higher We_g and Re_l surface breakup is observed. One case shows mixed or intermittent behavior and is classified as such. The breakup regime is found to be the same for both injectors. As regime map is plotted assuming that column breakup will dominate for lower values of We_g and Re_l and surface breakup at higher values. As clarified in (Wu et al., 1997), it is challenging to define a precise equation for the regime boundary based on a limited number of observations. Hence, an approximate boundary is marked, and it is hoped that in the future, more experimental and numerical results will be available to validate or improve this regime map.

In the above discussion, the injector geometry is found to be the governing parameter for jet morphology in the near-nozzle region. Whereas the far-field breakup behavior is controlled by We_g and Re_l. We_g in turn is governed by air crossflow. These observations give rise to some intriguing questions: Is the role of injector geometry limited only to the

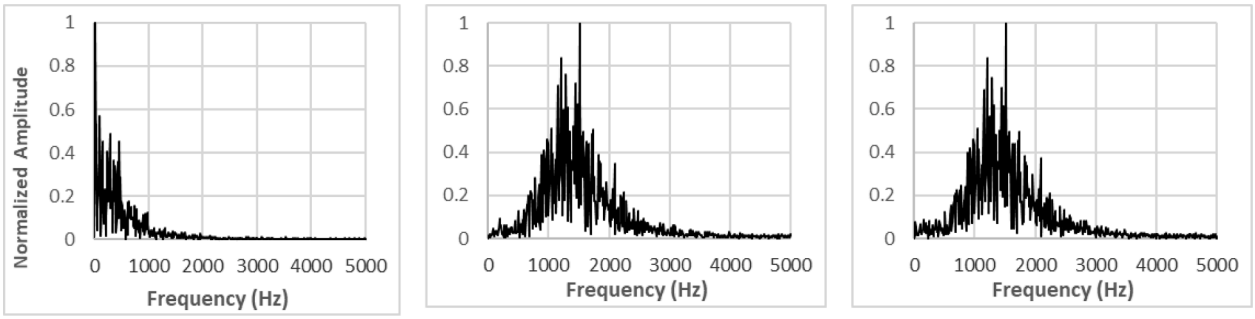

(i) J1-10, Mode 2 (ii) J1-10, Mode 3 (iii) J1-10, Mode 4

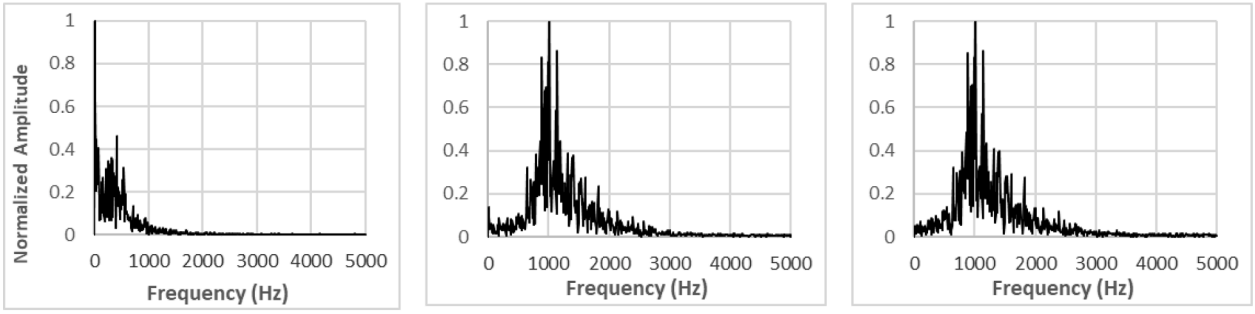

(iv) J1-100, Mode 2 (v) J1-100, Mode 3 (vi) J1-100, Mode 4

Fig. 8. PSD spectrum for J1-10 and J1-100 cases.

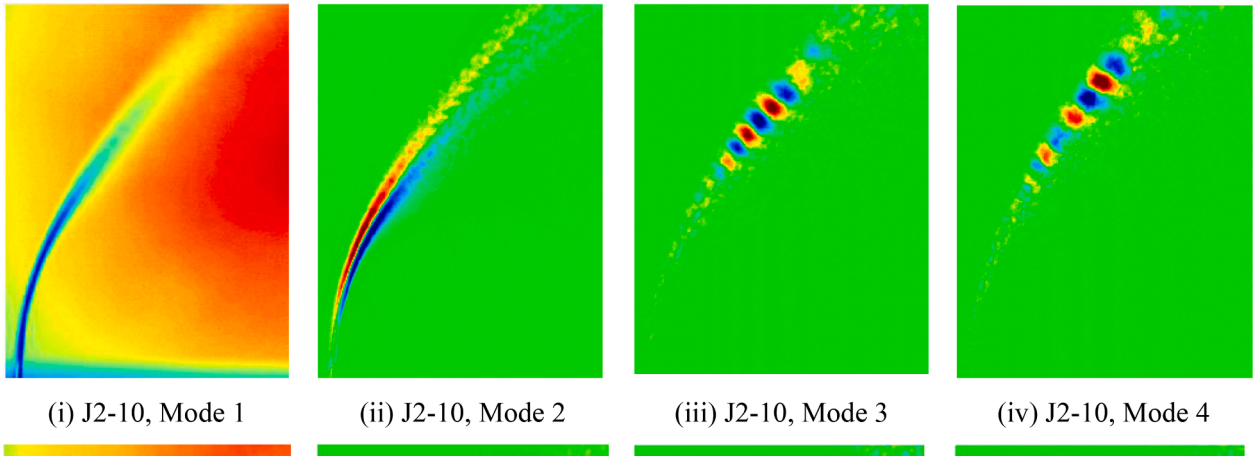

(i) J2-10, Mode 1 (ii) J2-10, Mode 2 (iii) J2-10, Mode 3 (iv) J2-10, Mode 4

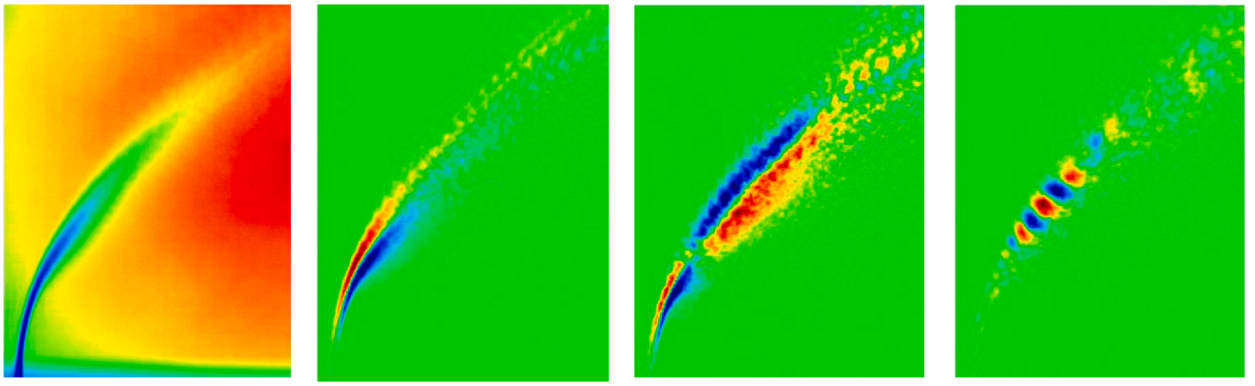

(v) J2-100, Mode 1 (vi) J2-100, Mode 2 (vii) J2-100, Mode 3 (viii) J2-100, Mode 4

Fig. 9. POD Mode shapes for J2-10 and J2-100 cases.

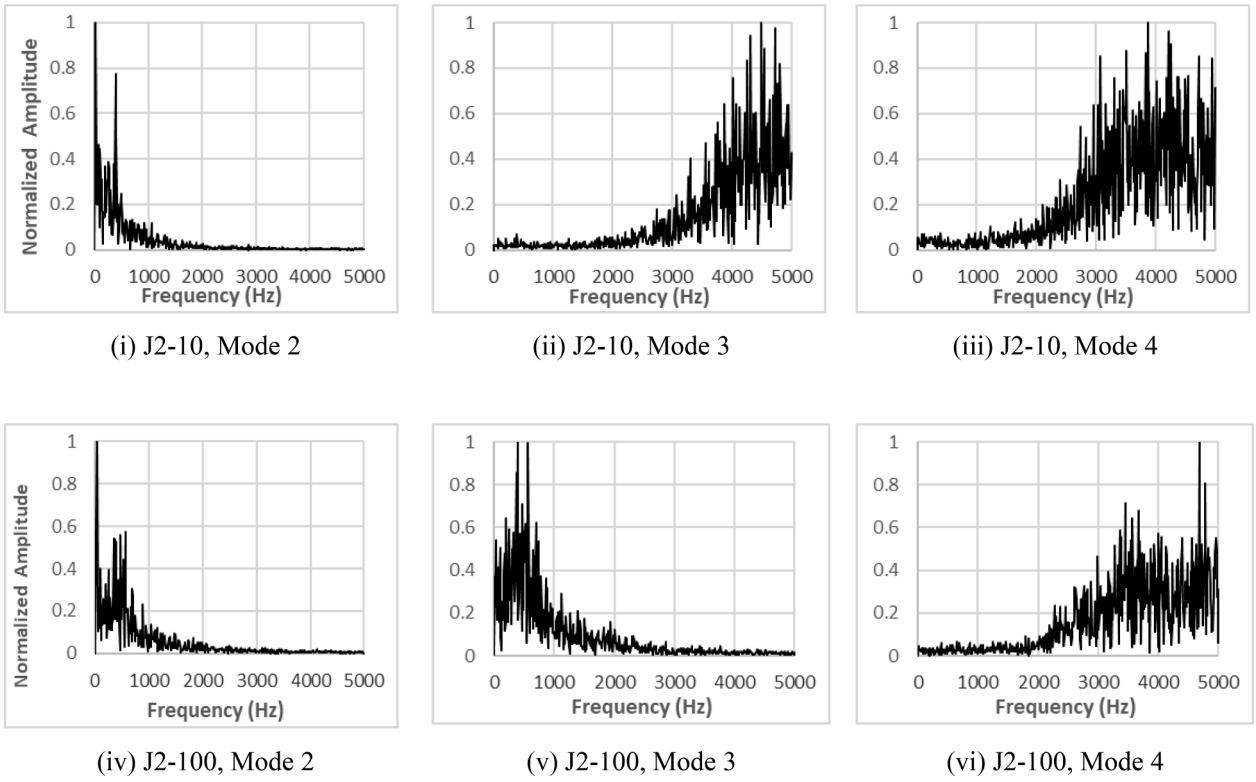

(i) J2-10, Mode 2 (ii) J2-10, Mode 3 (iii) J2-10, Mode 4

(iv) J2-100, Mode 2 (v) J2-100, Mode 3 (vi) J2-100, Mode 4

Fig. 10. PSD spectrum for J2-10 and J2-100 cases.

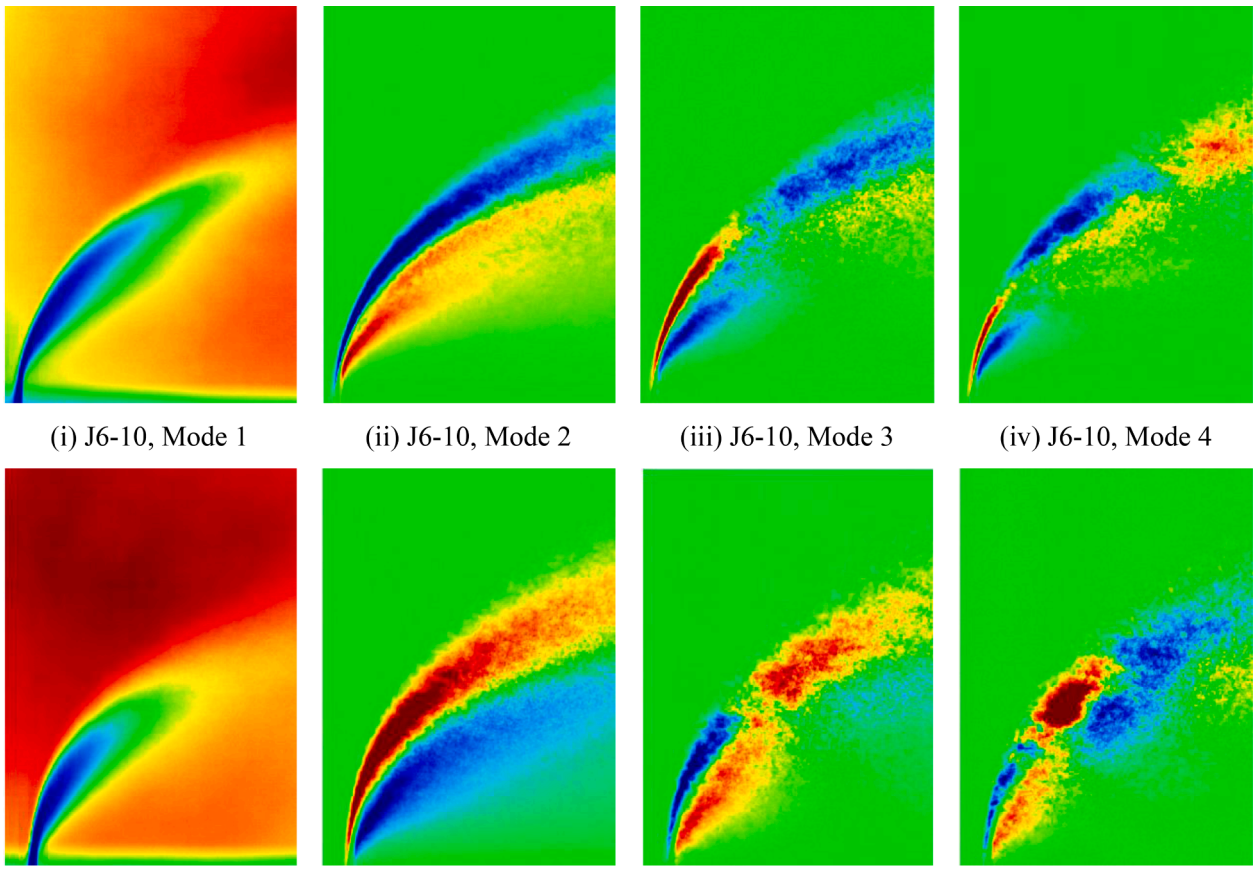

(i) J6-10, Mode 1 (ii) J6-10, Mode 2 (iii) J6-10, Mode 3 (iv) J6-10, Mode 4

(v) J6-100, Mode 1 (vi) J6-100, Mode 2 (vii) J6-100, Mode 3 (viii) J6-100, Mode 4

Fig. 11. POD Mode shapes for J6-10 and J6-100 cases.

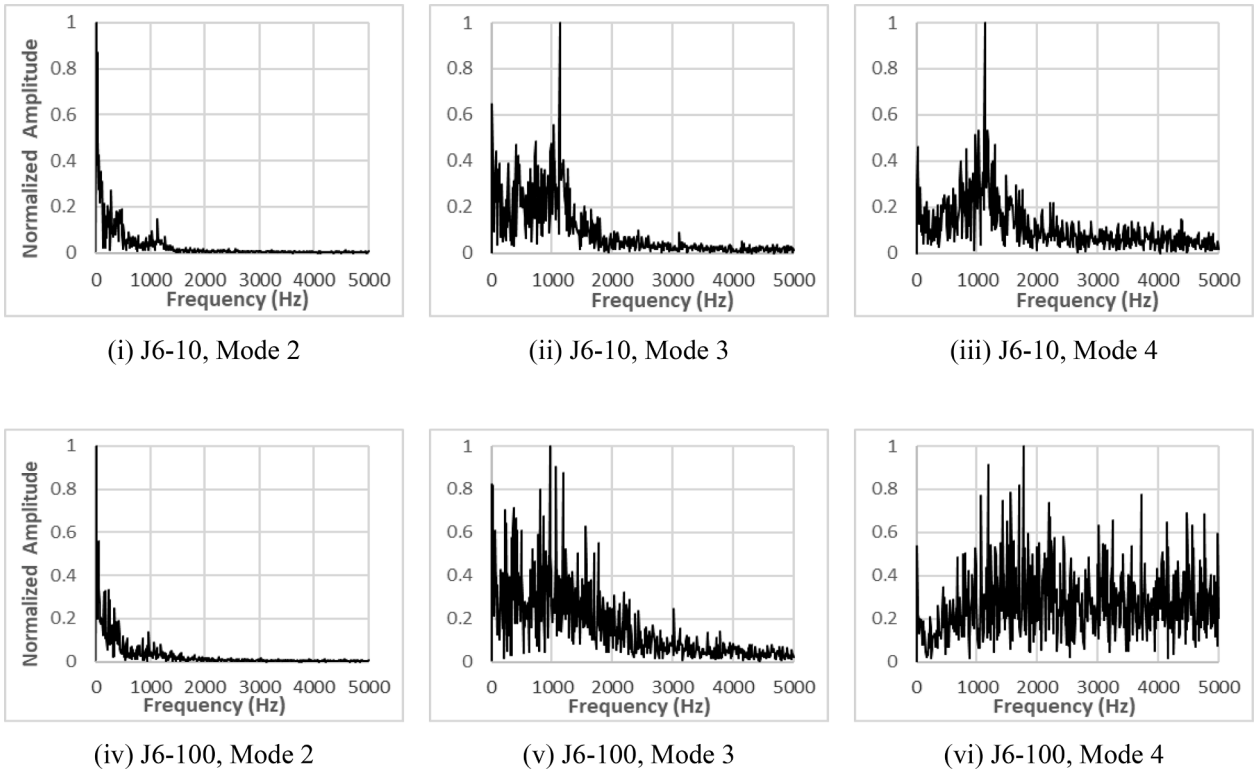

Fig. 12. PSD spectrum for J6-10 and J6-100 cases.

initial jet formation or does it also affect the jet breakup in crossflow? If it affects breakup, how that can be probed?

To further investigate the underlying process, POD analysis is carried out for the JICF cases discussed above. Fig. 7 shows the POD modes for J1-10 and J1-100, and Fig. 8 shows the corresponding PSD modes, highlighting dominant frequencies. The first POD mode is the average mode, which shows the mean jet trajectory. Since it is the average mode, its corresponding PSD is not shown. The mean trajectory of J1-10 (Fig. 7 (i)) and J1-100 (Fig. 7 (v)) look similar. However, the difference gets highlighted in higher modes. Mode 2 captures the jet oscillation about its mean position. It takes place at a peak frequency of around 500 Hz in both cases. However, jet oscillation in J1-100 (Fig. 7(vi)) is more pronounced as compared to J1-10 (Fig. 7 (ii)). Jet oscillation is an essential motion in LJIC and is observed in all the cases considered in this study. Generally, the jet oscillates at around 500 Hz for all the cases implying it to be a basic jet motion. POD modes 3 and 4 are similar and denote bag/ligament breakup and transport along the jet trajectory. Mode 3 (Fig. 8 (ii)) and mode 4 (Fig. 8 (iii)) for J1-10 show a peak of around 1500 Hz, whereas around 1000 Hz is observed for case J1-100 (Fig. 8 (v)). Bags and ligaments formed in J1-100 are larger than those formed in J1 (cf. Fig. 7). The third (Fig. 7 (vii)) and fourth (Fig. 7 (viii)) modes of J1-100 also show signatures of column oscillation. This stresses that the J1-100 jet is more unstable.

Moreover, jet oscillation exhibits multiple frequencies in PSD plots for both cases (Fig. 8), highlighting the complexity of the breakup process. For both J1-10 and J1-100, the jet is laminar. The difference due to L/D ratios is not as pronounced in this pair, as observed for other pairs discussed in the following sections.

Case J2 cases have the same Weber number as J1 cases. However, the values of Re_l and q are increased (cf. Table 1). The near-nozzle images from Fig. 3 demonstrate that the jet shows laminar behavior for J2-10 (Fig. 3 (i)) and turbulent characteristics for J2-100 (Fig. 3 (ii)). POD mode shapes and PSD plots for these cases are shown in Figs. 9 and 10, respectively. From Fig. 9, it is observed that the mean jet trajectory of J2-100 (Fig. 9 (ii)) is slightly shorter than J2-10 (Fig. 9 (i)) and is relatively more deflected in the crossflow direction. Column oscillation is more prominent in J2-100 (Fig. 9(vi)) than in J2-10 (Fig. 9 (ii)). J2-10 column also appears to penetrate more (cf. Mode 2 for both the cases – Fig. 9 (ii) and (vi)). Mode 3 (Fig. 9 (iii)) and mode 4 (Fig. 9(iv)) for J2-10 denote the ligament/ bag breakup and transport. This ligament breakup happens at a broadband spectrum of around 4000 Hz, as observed in PSD plots in Fig. 10 (Fig. 10(ii) and (iii)). On the other hand, mode 3 of J2-100 (Fig. 9 (vii)) shows jet flapping, a complex form of jet oscillation that occurs around the same frequency as the jet oscillation of Mode 2. It signifies the more complex and violent breakup behavior of J2-100. Jet flapping and its difference from jet oscillation are explained using a schematic in Appendix (Fig. A2). In jet oscillation, the jet oscillates above and below its mean position, when its extreme positions do not intersect. Whereas for jet flapping, the trajectories of extreme positions also intersect, as shown in Fig. A2. This can be attributed to the whiplash motion of the jet due to the breakup. Bag breakup is captured in the fourth POD mode of J2-100 (Fig. 9 (viii)), and this also shows a broadband spectrum between 3500 to 4500 Hz (Fig. 10 (vi)). PSD showing a broad range of frequencies indicates a more complex process involving multiple timescales.

POD mode shapes for J6-10 and J6-100 cases and shown in Fig. 11, and their PSD modes are shown in Fig. 12. Mode 1, denoting the mean jet trajectory appears to be shorter for J6-100 (Fig. 11(v)), as compared to J6-10 (Fig. 11 (i)). It is also more deflected in the crossflow direction. This behavior is consistent in all cases, that higher L/D injectors will have a more deflected and shorter average trajectory. J6 cases also exhibit the surface stripping of droplets which form a separate stream. The upper stream consists of a jet column and large ligaments following the jet trajectory. The lower stream comprises small droplets stripped off the jet surface. This behavior is depicted in Mode 2 (Figs. 11(ii), (vi)). This is the reason why Mode 2 of J6 cases is much broader than Mode 2 of all previous cases. Further, Mode 2 of J6-100 (Fig. 11 (vi)) is wider compared to J6-10 (Fig. 11 (ii)) since J6-100 has more unstable and higher droplet stripping. This aspect becomes clearer from the videos of high-speed images. This behavior getting captured in POD modes

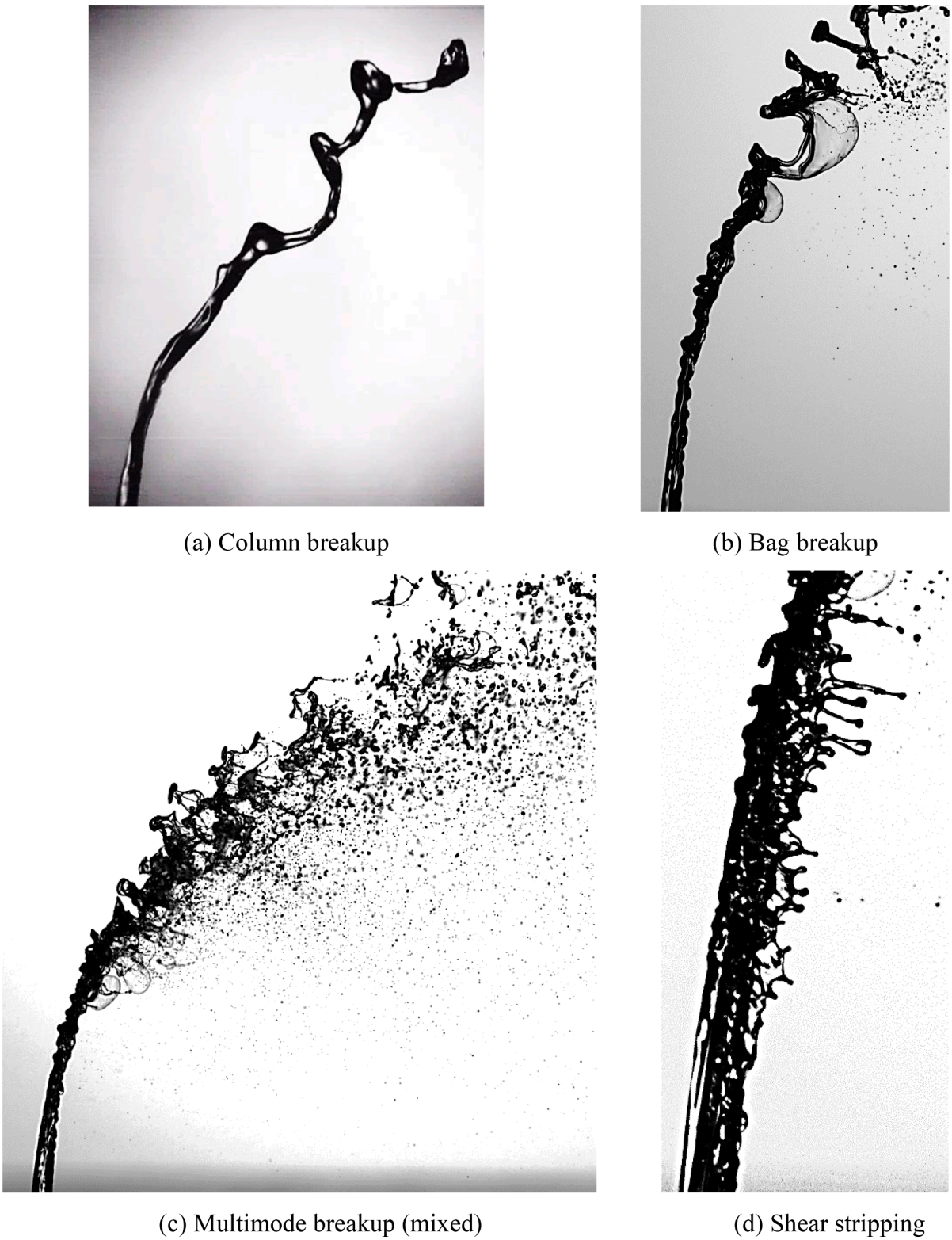

Fig. A1. Various breakup modes.

demonstrates the capability of POD to identify hidden features in a flow field. PSD of Mode 2 (Figs. 12 (i), (iv)) reveals a dominant peak near the zero frequency, which signifies contribution from the mean flow field. Mode 3 and 4 denote the jet flapping behavior in the near nozzle region and ligament transport in the far field. Mode 3 (Fig. 12(ii)) and mode 4 (Fig. 12 (iii)) of J6-10 show PSD peaks at around 1000 Hz. The same frequency was reported previously for ligament transport of J1 cases. However, the ligament transport and breakup process are more complex in J6-100, signified by the wide range of frequencies observed in mode 4 of J6-100 (Fig. 12 (vi)). Interestingly, the PSD spectrums have more clearly defined peaks for J1 cases (Fig. 8), while the frequency spectrum becomes wide for higher modes of J2 (Fig. 10) and wider for J6 (Fig. 12). It can be inferred that the breakup process becomes more complex with an increase of We_g and Re_l.

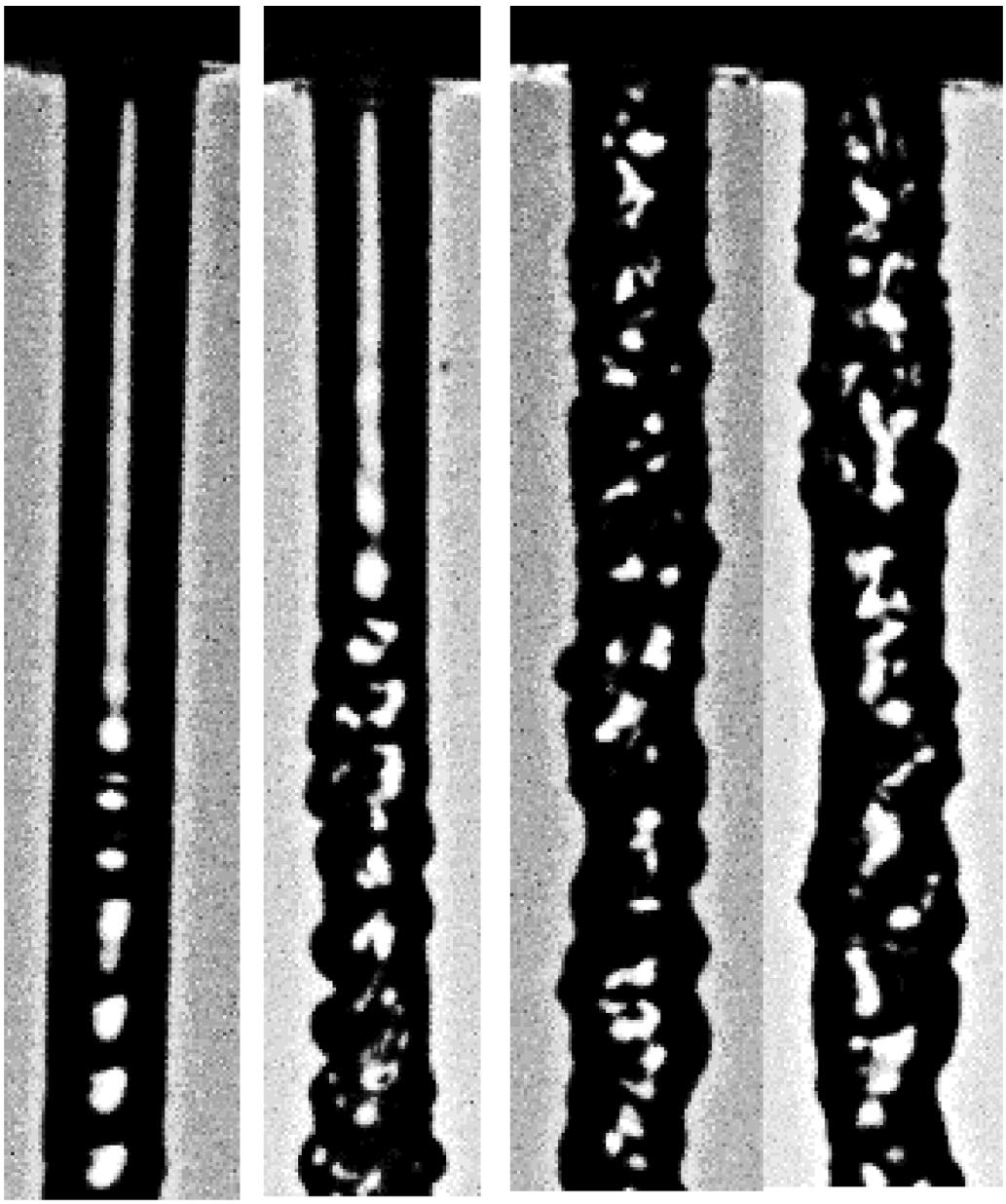

Fig. A2. Liquid jet at $Re_l = 5090$ for various L/D ratios.

Finally, DMD modes are also presented in Appendix (Fig. A5) for J1-10 and J1-100 cases. The DMD modes capture the mean flow field well. For higher modes, it shows signs of jet oscillation as seen in POD modes. However, it is more suitable for capturing small-scale motion as observed in Fig. A2, and POD seems to be suitable for capturing large-scale dominant features. However, more work is required to assess the applicability of both techniques to identify hidden structures.

3.2. Discussion

The effect of injector geometry is demonstrated in initial jet morphology, turbulent behavior, and breakup. Since the injector length is not sufficient to obtain a fully developed flow, a change in L/D will invariably cause a change in the liquid velocity profile. Further, the surface roughness of the injector will also play a role in the laminar to turbulent transition. Non-intrusive velocity measurement remains a key challenge in an experimental study. Some recent advances in computational modeling explore this aspect (Agarwal and Trujillo, 2020, Balaji et al., 2022). However, scanning the nozzle's internal geometry and capturing it accurately through grid points makes it a challenging task. High-fidelity atomizing simulations remain computationally expensive; it is challenging to use them in a practical or industrial configuration. Nonetheless, numerical modeling is expected to play a major role in future developments in this area of research (Balaji et al., 2022).

LJIC can also be probed through theoretical modeling. Models for surface waves seem to work well in predicting initial wave growth (Sinha, 2019). However, the present models do not explain the transient behavior observed in POD modes in the present study. This in part can be attributed to the rather simplistic assumption of linear stability theory, where viscous terms are neglected in dispersion relation (Sinha, 2019, Agarwal and Trujillo, 2018). It is observed that non-linear terms play a major role in determining jet breakup and subsequent atomization (Agarwal and Trujillo, 2018). Future studies on this aspect are expected

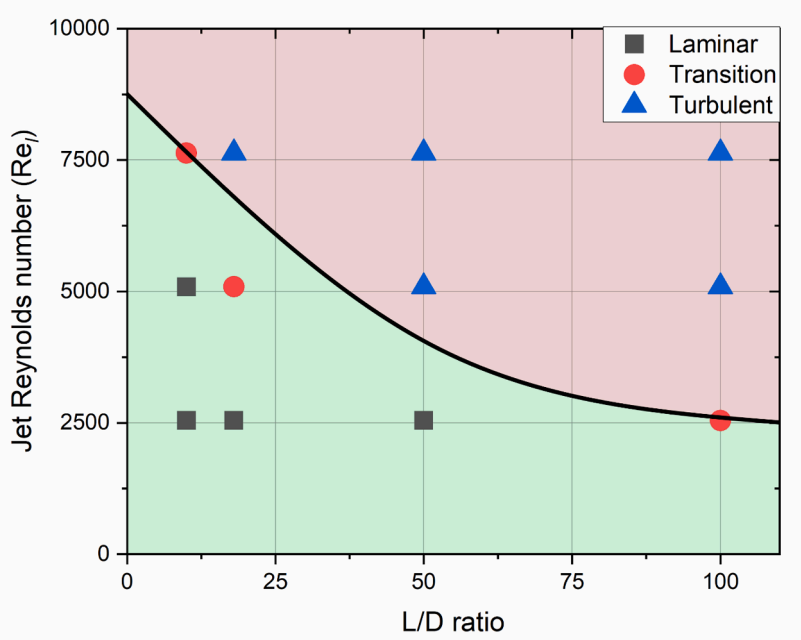

Fig. A3. Regime map for the straight jet at various L/D ratios and Reynolds number.

to aid the understanding of the jet structure and atomization in the context of LJIC.

4. Conclusion

The present study investigates liquid jet breakup in the presence of crossflow of air. Liquid Reynolds number varies from 2545 to 10180 to capture both laminar and turbulent jet behavior. The aerodynamic Weber number varied from 16 to 79 to observe different breakup modes. A regime map is proposed for jet breakup behavior. Injector L/D varies from 10 to 100 to study its effect on jet breakup. High-resolution, pulsed images are used to investigate the near-nozzle jet behavior. Time-resolved jet trajectory images are used to study the temporal evolution of breakup dynamics. Proper Orthogonal Decomposition of time-resolved images is used to probe jet stability. It is observed that the injector (L/D) ratio affects the jet stability and its eventual breakup in the presence of crossflow.

A general observation is that the jet from a higher (L/D) injector tends to be more unstable and disintegrates more rapidly; its trajectory is also more deflected in the crossflow direction. The POD modes and PSD spectra are also able to capture this trend. POD mode shapes show column oscillation and jet flapping occurring at higher amplitude for the jet with higher (L/D). Time-resolved videos also verify this observation. Sheet stripping is also amplified for higher (L/D). PSD spectra show an increase in high-frequency peaks, indicating the breakup to become more complex, and POD modes to be the superposition of several processes happening at different time scales with an increase in We_g and Re_l. The (L/D) ratio is believed to alter the velocity profile of the jet, which determines its stability. Future studies are planned to probe further the velocity profile and how it governs jet stability. Other geometric parameters like the type of entrance contraction ratio need to be investigated in detail to improve understanding of the breakup phenomenon.

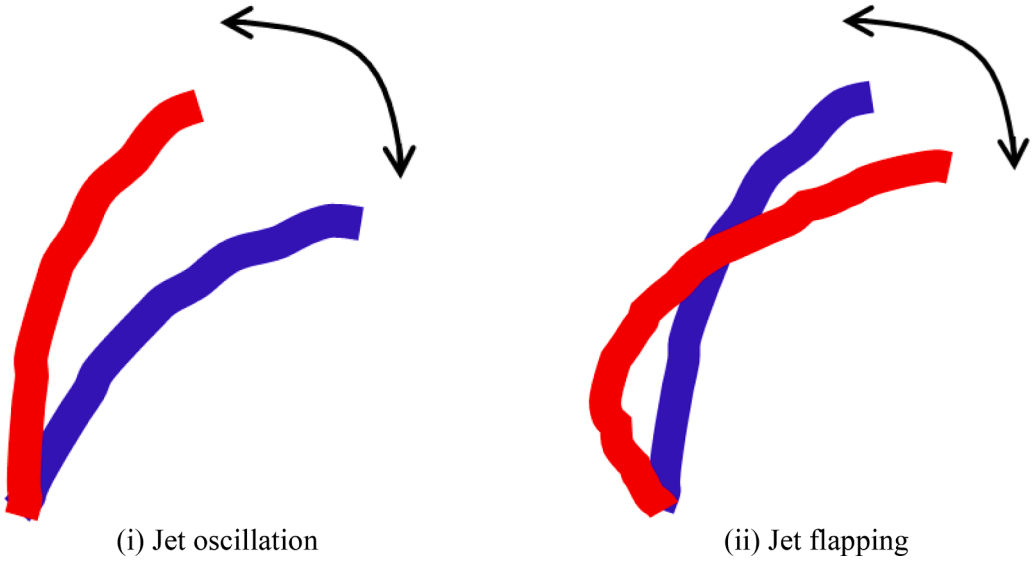

Fig. A4. Jet column oscillation and flapping.

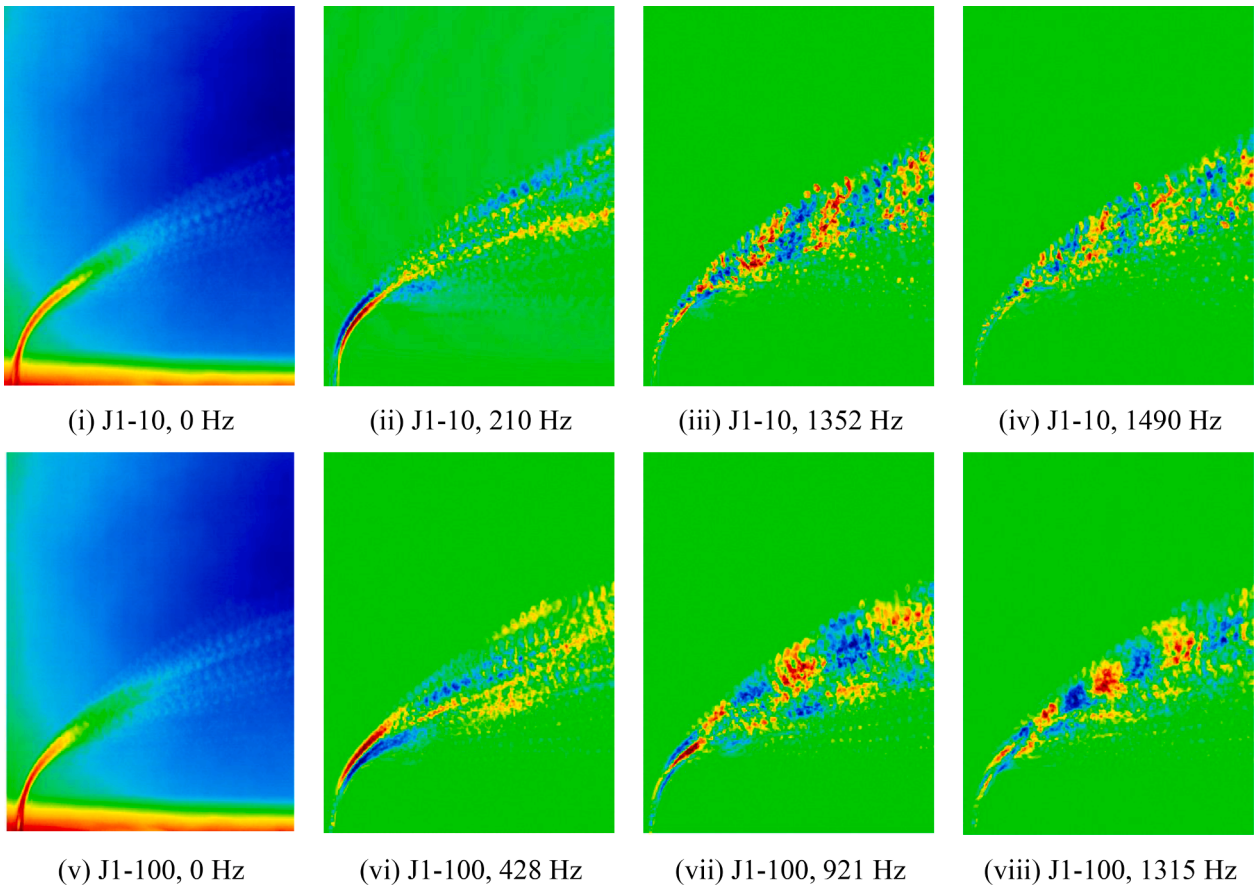

Fig. A5. DMD Mode shapes for J1-10 and J1-100 cases. The corresponding frequencies are also denoted.

Declaration of Competing Interest

The authors declare that they have no known competing financial interests or personal relationships that could have appeared to influence the work reported in this paper.

Acknowledgments

The author gratefully acknowledges the support provided by R. V. Ravikrishna (IISc Bangalore) for the experimental part of this work. The author would also like to acknowledge ARDB, Govt of India, for funding a part of this work.

Supplementary materials

Supplementary material associated with this article can be found, in the online version, at doi:10.1016/j.ijmultiphaseflow.2023.104497.

Appendix A

The following images are presented in the Appendix. Fig. A1 demonstrates the various breakup modes for LJIC configuration. Fig. A2 presents high-resolution images of a liquid jet for the near nozzle region injected in quiescent ambient (without crossflow). The images are for the same Re_l obtained using different injectors of varying L/D ratios. As observed, the L/D 10 jet appears laminar, while for larger L/D, the jet becomes unstable and fully turbulent for L/D 100. This demonstrates the impact of injector geometry on jet instability and eventual breakup. Examining more such cases, a regime map is formed classifying jets into laminar, turbulent, and transition cases. This map is shown in Fig. A3. Fig. A2 demonstrates schematically different jet column motions, viz, jet oscillation and jet flapping. Further, DMD results for LJIC cases are presented in Fig. A5. DMD for these cases captures small-scale structures and is not useful for examining large structures as observed in POD. DMD mode frequency is provided in the Fig caption.

References

Agarwal, A., Trujillo, MF., 2018. A closer look at linear stability theory in modeling spray atomization. Int. J. Multiph. Flow 109, 1–13.
Agarwal, A., Trujillo, M.F., 2020. The effect of nozzle internal flow on spray atomization. Int. J. Engine Res. 21 (1), 55–72.
Arienti, M., Soteriou, MC., 2009. Time-resolved proper orthogonal decomposition of liquid jet dynamics. Phys. Fluids 21 (11), 112104.
Balaji, S., Kumar, A., Pratap, A., and Sinha, A., (2022) "Surface Breakup of Liquid Jet – Insights from a DNS study", *ILASS Asia, 22nd Annual Conference on Liquid Atomization and Spray Systems*, 2022 IIT Indore.
Becker, J., Hassa, C., 2002. Breakup and atomization of a kerosene jet in crossflow at elevated pressure. Atomization Sprays 12 (1-3).
Behzad, M., Ashgriz, N., Karney, B.W., 2016. Surface breakup of a nonturbulent liquid jet injected into a high pressure gaseous crossflow. Int. J. Multiph. Flow 80, 100–117.
Berkooz, G., Holmes, P., Lumley, J.L., 1993. The proper orthogonal decomposition in the analysis of turbulent flows. Ann. Rev. Fluid Mech. 25 (1), 539–575.
Brassard, D., Ferchichi, M., 2005. Transformation of a polynomial for a contraction wall profile. J. Fluids Eng. 127 (1), 183–185.
Broumand, M., Birouk, M., 2016. Liquid jet in a subsonic gaseous crossflow: recent progress and remaining challenges. Progr. Energy Combust. Sci. 57, 1–29.
Brown, C.T., and V.G. McDonell. "Near field behavior of a liquid jet in a crossflow." *Proceedings of the ILASS Americas, 19th Annual Conference on Liquid Atomization and Spray Systems*. 2006.
Gong, C., Ou, M., Jia, W., 2019. The effect of nozzle configuration on the evolution of jet surface structure. Res. Phys. 15, 102572.
Herrmann, M., 2010. Detailed numerical simulations of the primary atomization of a turbulent liquid jet in crossflow. J. Eng. Gas Turbines Power 132 (6).
Lee, K., et al., 2007. Primary breakup of turbulent round liquid jets in uniform crossflows. AIAA J. 45 (8), 1907–1916.
Li, X., Soteriou, M.C., 2016. High fidelity simulation and analysis of liquid jet atomization in a gaseous crossflow at intermediate Weber numbers. Phys. Fluids 28 (8), 082101.

Liang, Y.C., et al., 2002. Proper orthogonal decomposition and its applications—Part I: Theory. J. Sound Vib. 252 (3), 527–544.
Madabhushi, R.K., et al. “On the breakup regime map of liquid jet in crossflow.” ILASS Americas, *19th Annual Conference on Liquid Atomization and Spray Systems*, Toronto, Canada. 2006.
Mashayek, A., Ashgriz, N., 2011. Atomization of a liquid jet in a crossflow. Handbook of Atomization and Sprays. Springer, Boston, MA, pp. 657–683.
Mazallon, J., Z. Dai, and G. Faeth. "Aerodynamic primary breakup at the surface of nonturbulent round liquid jets in crossflow." *36th AIAA Aerospace Sciences Meeting and Exhibit*. 1998.
McCarthy, M.J., Molloy, N.A., 1974. Review of stability of liquid jets and the influence of nozzle design. Chem. Eng. J. 7 (1), 1–20.
Mehta, R.D., Bradshaw, P., 1979. Design rules for small low speed wind tunnels. Aeronaut. J. 83 (827), 443–453.
Ng, C.-L., Sankarakrishnan, R., Sallam, K.A., 2008. Bag breakup of nonturbulent liquid jets in crossflow. Int. J. Multiph. Flow 34 (3), 241–259.
No, S.-Y., 2015. A review on empirical correlations for jet/spray trajectory of liquid jet in uniform cross flow. Int. J. Spray Combust. Dyn. 7 (4), 283–313.
Portillo, J.E., Collicott, S.H., Blaisdell, G.A., 2011. Measurements of axial instability waves in the near exit region of a high speed liquid jet. Phys. Fluids 23 (12), 124105.
Sallam, K.A., et al. “Breakup of turbulent and nonturbulent liquid jets in gaseous crossflows.” *44th AIAA Aerospace Sciences Meeting and Exhibit*. 2006.
Sallam, K.A., Aalburg, C., Faeth, G.M., 2004. Breakup of round nonturbulent liquid jets in gaseous crossflow. AIAA J. 42 (12), 2529–2540.
Schmid, P.J., 2010. Dynamic mode decomposition of numerical and experimental data. J. Fluid Mech. 656, 5–28.
Sinha, A., et al., 2015. Airblast spray in crossflow–structure, trajectory, and droplet sizing. Int. J. Multiph. Flow 72, 97–111.
Sinha, A., Ravikrishna, R.V., 2019. Experimental studies on structure of airblast spray in crossflow. Sādhanā 44 (5), 1–13.
Sinha, A., 2019. Surface waves on liquid jet in crossflow: Effect of injector geometry. AIAA J. 57 (10), 4577–4582.
Sirovich, L., 1987. Turbulence and the dynamics of coherent structures. I. Coherent structures. Q. Appl. Math. 45 (3), 561–571.
Stenzler, JN., et al., 2006. Penetration of liquid jets in a cross-flow. Atomization Sprays 16 (8).
Taira, K., et al., 2017. Modal analysis of fluid flows: an overview. AIAA J. 55 (12), 4013–4041.
Taira, K., et al., 2020. Modal analysis of fluid flows: applications and outlook. AIAA J. 58 (3), 998–1022.
Tretola, G., Vogiatzaki, K., Navarro-Martinez, S., 2021. Effect of the density ratio variation on the dynamics of a liquid jet injected into a gaseous crossflow. Phys. Fluids 33 (9), 092120.
Wu, P.-K., et al., 1997. Breakup processes of liquid jets in subsonic crossflows. J. Propuls. Power 13 (1), 64–73.
Wu, P.-K., et al., 1998. Spray structures of liquid jets atomized in subsonic crossflows. J. Propuls. Power 14 (2), 173–182.
Wu, P-K., Miranda, R.F., Faeth, G.M., 1995. Effects of initial flow conditions on primary breakup of nonturbulent and turbulent round liquid jets. Atomization Sprays 5 (2).